Storm-time equatorial magnetospheric ion temperature derived from TWINS ENA flux

R. M. Katus[1,2,3], A. M. Keesee[2], E. Scime[2], M. W. and Liemohn[3]

1. Department of Mathematics, Eastern Michigan University, Ypsilanti, MI, USA

2. Department of Physics and Astronomy, West Virginia University, Morgantown, WVU, USA

3. Department of Climate and Space Sciences and Engineering, University of Michigan, Ann Arbor, MI, USA

Corresponding author email: rkatus@umich.edu

Key points:

- We derive and statistically examine storm-time equatorial magnetospheric ion temperatures from TWINS ENA flux

- The TWINS ion temperature data is validated using Geotail and LANL ion temperature data

- For moderate to intense storms the widest (in MLT) peak in nightside ion temperature is found to exist near 12 R_E

Abstract

The plasma sheet plays an integral role in the transport of energy from the magnetotail to the ring current. We present a comprehensive study of the of equatorial magnetospheric ion temperatures derived from Two Wide-angle Imaging Neutral-atom Spectrometers (TWINS) Energetic Neutral Atom (ENA) measurements during moderate to intense ($Dst_{peak} < -60$ nT) storm times between 2009 and 2015. The results are validated using ion temperature data derived from the Geotail low energy particle energy analyzer (LEP-EA) and the Los Alamos National Laboratory magnetospheric plasma analyzer (LANL-MPA). The ion temperatures are analyzed as a function of storm time, local time, and Lshell. We perform a normalized superposed epoch analysis of 48 geomagnetic storms and examine the spatial and temporal evolution of the plasma as a function of storm phase. This analysis illustrates the spatial and temporal variation of the ions from the plasma sheet into the inner magnetosphere. We find that the ion temperature increases approaching the storm peak. This enhancement has the largest MLT extent near 12 R_E distance downtail.

1. Introduction

A geomagnetic storm is the magnetospheric reaction to solar activity. Energy is transferred from the solar wind into the magnetosphere through a cycle described in the Dungey model [*Dungey,* 1961]. During storms, the plasma sheet plays a crucial role in the transport of hot (2-20 keV range), moderately dense (0.3-3.0 cm^3) plasma [*Baumjohann et al.,* 1989; *Baumjohann,* 1993; *Zhang et al.,* 2006] from the near-equatorial magnetotail into the inner magnetosphere [*Korth et al.,* 1999; *Korth and Thomsen*, 2001; *Friedel et al.,* 2001]. This injection is the main source of the ring current [e.g., *Smith et al.,* 1979; *Chen et al.,* 1994; *Kozyra et al.,* 1998b; *Korth et al.,* 1999; *Ebihara et al.,* 2005; *Denton et al.,* 2005, 2006].

Geosynchronous plasma observations have historically been available via seven Los Alamos National Laboratory (LANL) satellites. These satellites carry magnetospheric plasma analyzer (MPA) instruments near the geographic equatorial plane and make observations at distinct

geographic longitudes [*Bame et al., 1993*].

Observations from these satellites provided data that allowed many of the studies that define the state of knowledge of the magnetospheric ion temperature at geosynchronous orbit. Many studies over the last two decades have explored the relationship of near-Earth plasma characteristics to geomagnetic activity using the LANL-MPA data set [e.g., *Birn et al*., 1997; *Borovsky et al.*, 1997; *Thomsen et al*., 2003; *Lavraud et al.*, 2005; *Liemohn et al.*, 2008]. In particular, *Denton et al.* [2005] examined LANL MPA data as a function of local time using superposed epoch analysis. They demonstrated the local time dependence of transport of the plasma sheet plasma into the inner magnetosphere and the simultaneous changes in plasma temperature and pressure.

Zhang et al. [2006] examined the source of the storm-time ring current using the LANL MPA parallel and perpendicular ion temperature as a function of local time using superposed epoch analysis. They investigated different storm categories based on the typical variations of hot-ion fluxes (at the energies of 30, 17, 8, and 1 keV), density, temperature, entropy, and temperature anisotropy. They found that during solar minimum the nightside and afternoon sector temperature are generally greater than those that occur during solar maximum. Moreover, storms that occur during solar maximum demonstrate no clear temperature boost. Furthermore, the hot ions are isotropic on the nightside but anisotropic close to noon.

Denton and Borovsky [2008] used LANL MPA ion temperature data during CIR-driven storms in a superposed epoch analysis with convection onset as epoch zero. They demonstrate that preceding the onset of convection, the plasma sheet hot ion densities are greater on the nightside than the dayside. Subsequent the onset of convection, the ion density grows showing the transfer of material from the tail into geosynchronous orbit.

Other studies have examined the plasma sheet ion temperature using observations from the Geotail spacecraft. *Terasawa et al.* [1997] conducted a statistical examination of the Geotail plasma moments in the near-Earth plasma sheet. They found that during periods of northward IMF the plasma sheet becomes cold and dense. *Ohtani et al.* [2004] used the Geotail

observations to show that during substorms the ion temperature rises for the earthward flow and falls for the tailward flow. *Wang et al.* [2006] investigated the equatorial distributions of ions from Geotail during steady periods of northward and southward IMF. They found that during northward IMF the near-Earth plasma sheet exhibits a dawn-dusk temperature asymmetry with greater temperature on the dusk side. While these studies and many others have set the foundation for understanding the transport of plasma in the magnetosphere, the use of single-to-multipoint measurements produces several large gaps. In order to fully understand the complex temporal and spatial variation of plasma in the magnetosphere a more complete view is required.

Energetic Neutal Atom (ENA) imaging observes the global dynamics of the magnetosphere via detection of energetic neutrals produced during charge exchange [e.g. Krimigis et al., 1975; Roelof et al., 1985; Roelof, 1987; Henderson et al., 1999]. The Two Wide-angle Imaging Neutral-atom Spectrometers (TWINS) is the first stereoscopic, magnetospheric ENA imager [McComas et al*., 2009; Goldstein and McComas, 2013*]. A technique developed to calculate ion temperatures from ENA measurements [*Scime et al.*, 2002; *Keesee et al.*, 2011] provides the opportunity for studying the global behavior of such temperatures during geomagnetic storms.

Keesee et al. [2012] examined plasma sheet ion temperatures derived from remotely detected TWINS ENA Flux and found higher temperatures in high speed stream (HSS) driven storms than coronal mass ejection (CME) driven events. *Keesee et al.* [2014] conducted a superposed epoch analysis of TWINS derived ion temperatures during CME and HSS storms. They found that near the beginning of intense CME-driven storms, quick temperature increase occurs due to adiabatic compression. In this study we will present a robust new data set containing TWINS ENA flux derived ion temperature data for 48 moderate to intense (Dst_{min} < -60 nT) geomagnetic storms with 10 minute resolution from July 2009 to December 2015. While TWINS can make images with 1- minute resolution, 10- minute resolution is used for better counting statistics. We then statistically examine and validate the spatial and temporal evolution of the storm time magnetospheric ion temperature. We find that the ion temperature increases

approaching the storm peak. This enhancement has the largest MLT extent near 12 R_E distance downtail.

2. Ion Temperature Data

The NASA TWINS mission consists of two satellites in high-inclination Molniya orbits that are offset to provide near-continuous coverage [*McComas et al.*, 2009]. Each satellite includes an energetic neutral atom (ENA) imager, Lyman- α detectors, and in situ monitors. The ENA instruments were described by *McComas et al.* [2013]. They have two time of flight (TOF) sensor heads with energy ranging between ~1 and 100 keV/q that are offset by ±15° to give a ~140° view in one spatial dimension. The instrument sits on an actuator that offers the second spatial dimension, resulting in images with 4° x 4° resolution every 60 s. An instrument response model is used to sort the data into actuation angle, polar angle, and TOF bins. In this study, we assume all ENAs are hydrogen to convert the TOF bins into 11 energy bins with central energies of 2 to 24 keV with $\Delta E/E = 1$ (e.g., a bin with central energy of 12 keV includes energies from 6 keV to 18 keV). Data is processed using a statistics-based smoothing algorithm [*McComas et al.*, 2012]. Intervals containing angular uncertainty and sun contamination are removed.

Two-dimensional ion temperature maps are then created from the TWINS satellite data by applying the methods previously validated with in situ measurements [e.g. *Scime et al.*, 2002; *Keesee et al.*, 2014]. ENAs are created by charge exchange collision between a cold neutral and an energetic ion. The measured ENA intensity, j_{ENA} (with units of (cm^2 sr s eV)$^{-1}$), depends on the ion intensity, j_{ion}, the neutral density, n_n, and the energy-dependent charge exchange cross-section, σ_{cx}, [*Freeman and Jones*, 1974], by

$$J_{ENA}\left(E,\vec{u}\right) = \sigma_{cx}\left(E\right)\int_{0}^{\vec{R}}\left(n_n\left(\vec{r}(s)\right)j_{ion}\left(\vec{r}(s),E,\vec{u}\right)\exp\left(-\int_{0}^{\vec{r}(s)}\alpha(s')ds'\right)ds\right). \qquad (1)$$

The integral is performed along the LOS from the location of ENA emission, $\vec{r}$, to the location of the satellite, $\vec{R}$, with $\vec{r}(s) = \vec{r} + \vec{u}s$ and $\vec{u}$ is a unit vector along the LOS. Attenuation of ENAs
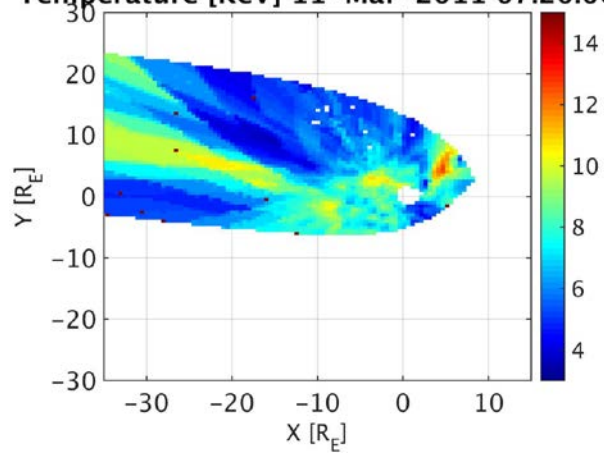
due to additional collisions or ionization along the path from the origination of the ENA to the instrument is accounted for by the integral over $\alpha(s')$. This integral is approximately zero for regions without recombination, significant scattering, etc., which is true for the magnetosphere beyond a few Earth radii [*Roelof and Skinner*, 2000]. Assuming a Maxwellian distribution for the parent ion population, the measured spectrum will be dominated by emission from the hottest region along the LOS [*Hutchinson*, 1987], yielding

$$J_{ENA} \approx \frac{\sigma_{cx}(E)E\xi n_n(r^*)n_i(r^*)}{\sqrt{2m_i}\left(\pi T_i(r^*)\right)^{3/2}} exp\left(\frac{-E}{T_i(r^*)}\right) \tag{2}$$
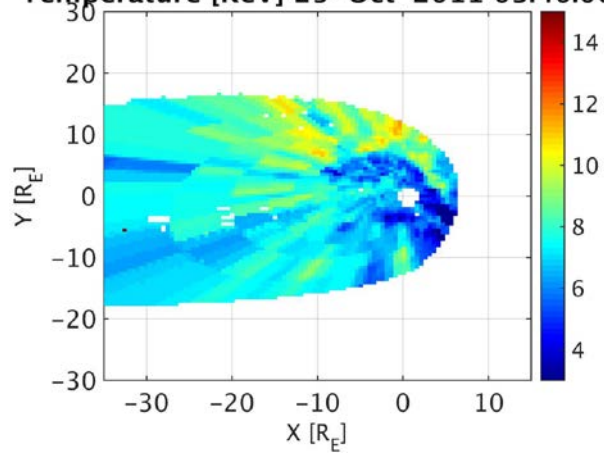
where r^* is the location of the hottest region along the LOS and ξ is a characteristic width of the hottest region. In our method of direct determination of ion temperature, the peak ion temperature along the line-of-sight is determined from fits of Eq. 2 to the ENA energy spectra.

Temperature [KeV] 11-Mar-2011 07:20:00

Temperature [KeV] 25-Oct-2011 03:40:00

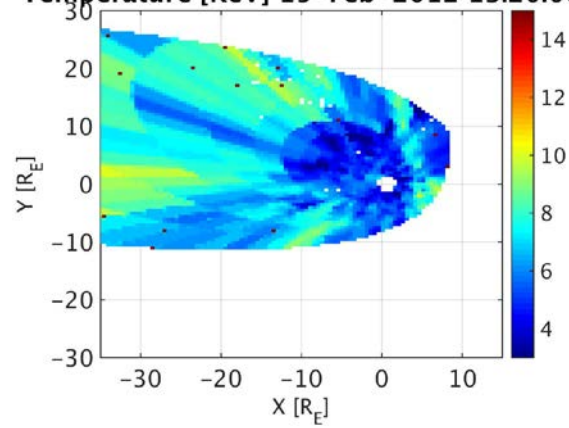Temperature [KeV] 15-Feb-2012 13:20:00

Figure 1. Three examples of the TWINS equatorial magnetospheric ion temperature maps at different times. The xy-axis describes the GSM coordinates with z=0 and the color describes the temperature.

ENA flux is assigned to the *xy*-plane (GSM coordinates) using a LOS mapping under the assumption that the central plasma sheet is the hottest point along the LOS [*Hughes*, 1995]. To account for the increasing field of view (FOV) with increasing distance from Earth, the FOV of each pixel in an ENA image is projected along the LOS to determine with which bins in the equatorial plane the FOV intersects. The ENA emissivity is then divided proportionally among the equatorial plane bins, and an average emissivity for each bin is found by dividing the total emissivity by the number of pixel FOVs intersecting that bin. Bins that fall outside of a modelled magnetosphere boundary [*Shue et al.*, 1997] are ignored. An ion temperature is calculated for each equatorial plane bin by fitting Equation 2 to the data. This method has been validated through comparisons with in situ measurements [*Scime et al.*, 2002; *Keesee et al.*, 2008].

Equatorial magnetospheric ion temperature results found using this method for three distinct storm-time snapshots are shown in Figure 1. The xy-axes describe GSM coordinates with z=0. The sun (12 MLT hours) is to the right along y=0 and x > 0. Midnight (24 MLT hours is to the left along y=0 x < 0. Dawn (6 MLT hours) is down, y < 0 and x = 0. Dusk is up, y > 0 and x = 0.

Figure 1 highlights several distinct features in the resulting magnetospheric ion temperature. First, we can see the global nature of the data set, providing spatial resolution at a given time not enabled by in situ measurements. This view also provides information about the temporal progression of medium energy plasma (2 to 32 keV) from the near-Earth tail to the inner magnetosphere when sequential time intervals are considered. Typically, there are higher temperatures on the dusk side (as seen on March 11, 2011 and February 15, 2012), a common result of the full storm time data set. Furthermore, each of the three images in Figure 1 have higher temperatures downtail in the plasma sheet. Additionally, the top plots show larger

temperatures on the near-Earth, nightside extending from the plasma sheet into the inner magnetosphere.

Figure 1 shows some limitations of this method, including the projection of the data leading to longer FOV and larger bins (reduced spatial resolution) in the tail. Another difficulty is displayed in the bottom panel plot showing February 15, 2012 and possibly in the middle plot as well showing October 25, 2011. The jump from lower to higher temperatures on the dusk side is an instrumental effect, caused by differences in the charge particle rejecting collimators. The collimator voltages are different, which allows different parts of the high-energy ion distribution into the two sensors. [*McComas et al*., 2009; 2012].

3. Normalized Superposed Epoch Analysis

Superposed epoch analysis (SEA) is frequently applied to uncover the characteristic behavior of a set of events [e.g. *Taylor et al.,* 1994]. This study applies SEA with a normalized epoch timeline [*Katus et al.,* 2013; *Katus and Liemohn* 2013; *Katus et al*., 2015] using multiple epoch markers to maintain information at each storm phase. These epoch markers are defined using an automated procedure to identify the start and end of each phase.
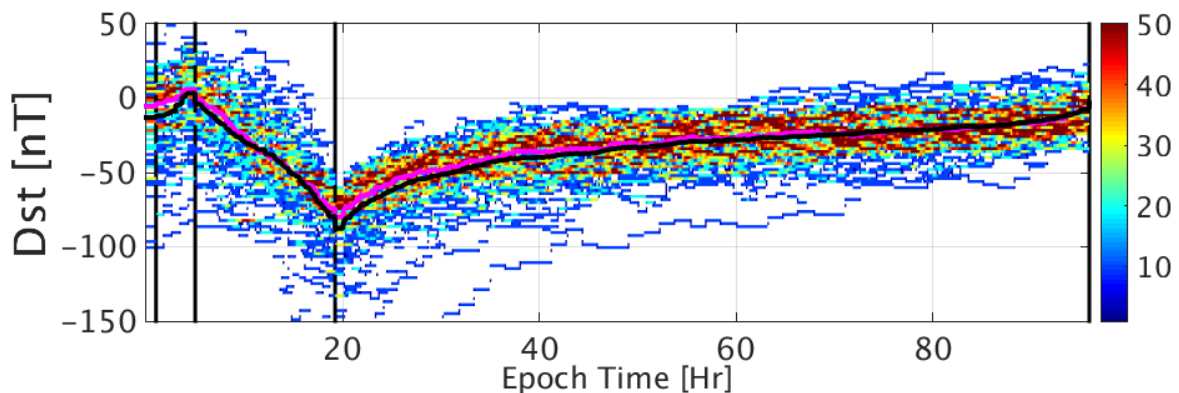
In this study we use all 48 of the storms between July 2009 and December 2015 with Dst_{peak} < -60 nT and at least 1 hour of available TWINS ENA flux data. The automated procedure then searches *Dst* for the time of the storm peak (Dst minimum). From there, the procedure determines the conclusion of the recovery using the highest Dst within the subsequent 4 days. Afterwards, the procedure determines the start of the main phase using the highest Dst within the day preceding to the storm peak. A storm sudden commencement (SSC) is not required in this work. Therefore, to include as many storms as possible, we attach an initial phase. Whether or not the initial phase contains a SSC, it can be used to describe the pre-storm geomagnetic conditions. The automated procedure defines the beginning of the initial phase as the sharpest Dst enhancement within the eight hours prior to the start of the main phase. Lastly, one hour

before the start of the initial phase is added to the start of the timeline in order provide information regarding the introductory condition of the magnetosphere.

The storm phase markers that were found using the automated procedure are then used to calculate the mean duration of each storm phase. For all moderate to intense geomagnetic storms we find that the average length of the initial phase is 3.97 hours, of the main phase is 14.23 hours, and of the recovery phase is 76.68 hours. The mean durations found for this study are consistent with these found in previous studies [*Pulkkinen et al.* 2007, *Ilie et al.* 2008, and *Katus et al.* 2013]. The epoch timeline is then normalized preforming linear interpolation. The normalization results in either expands or compresses the duration of the individual storm phase to match the mean duration.

4. Two Sample T Test

In this study we will want to show that the ion temperature for different magnetospheric regions are statistically significantly different. This study applies a two-sample T Test to compare the means from two independent data samples. T Tests assess the null hypothesis, that the two sets of data have equal population means. The null hypothesis is rejected if the absolute value of T is larger than a critical value at a given significance level.
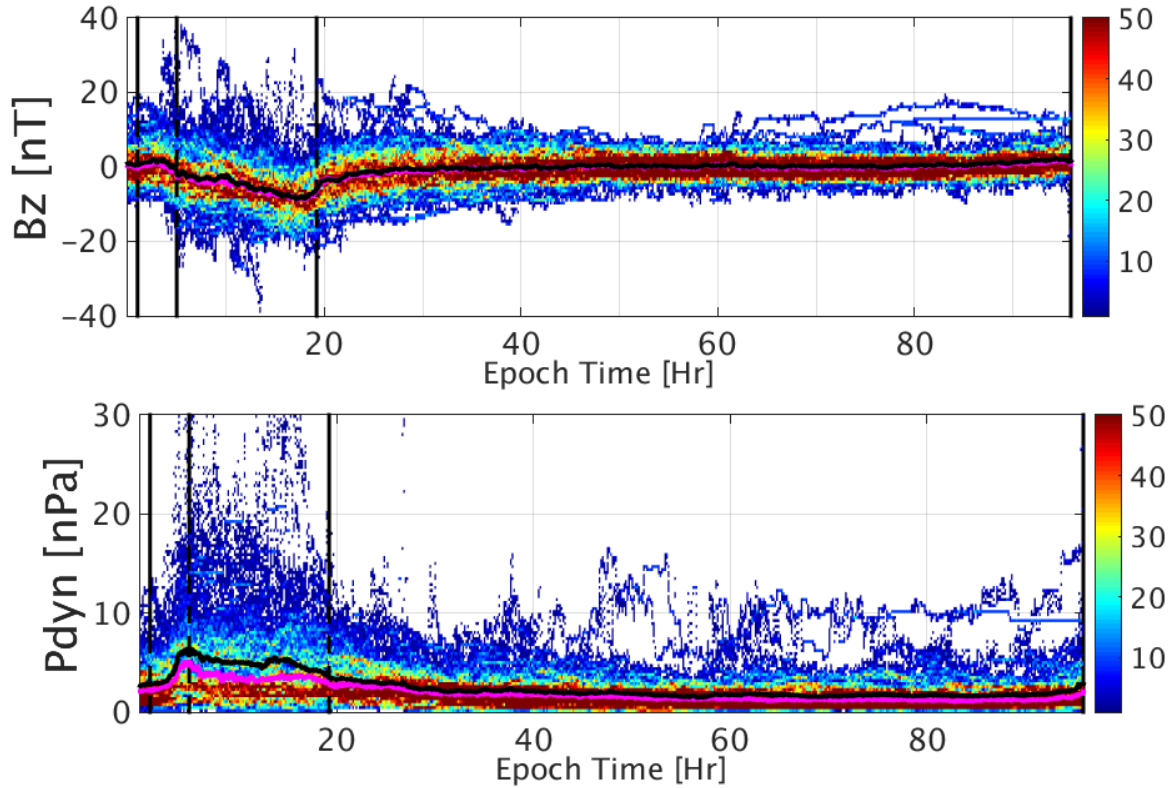
Figure 2. Normalized superposed epoch results for (top) Dst, (center) IMF Bz, (bottom) Solar wind dynamic pressure. The color describes the number of points in each bin. The black vertical lines describe the beginning or end of each storm phase. The black and pink lines following epoch time describe the mean and median of the data, respectively.

To simplify the result, we will follow the method used in *Katus et al.* [2016], which assessed the H value and P value. The H value defines the decision for the null hypothesis. The value of H = 0 indicates that we do not reject the null hypothesis at a 5% significance level. The value of H = 1 reveals that we reject the null hypothesis (the means are not equal). The P value is then defined as the probability that H was found due to random chance. Therefore a combination of H = 1 and a small P value demonstrates a convincing rejection of the null hypothesis, i.e., the means are statistically significantly different.

5. Results

Typical storm dynamics are presented in Figure 2 using the disturbance storm-time index (*Dst*), the z component of the interplanetary magnetic field (IMF B_Z), and the solar wind dynamic pressure (Pdyn). The colorbar describes the number of points in each bin. In each plot there are 100 bins along the y-axis and 15 minute bins along the x-axis. The black vertical lines, from left to right, indicate the times of the storm sudden commencement, the beginning of the main phase, and the storm peak. The black and pink lines following epoch time describe the mean and median of the data, respectively.
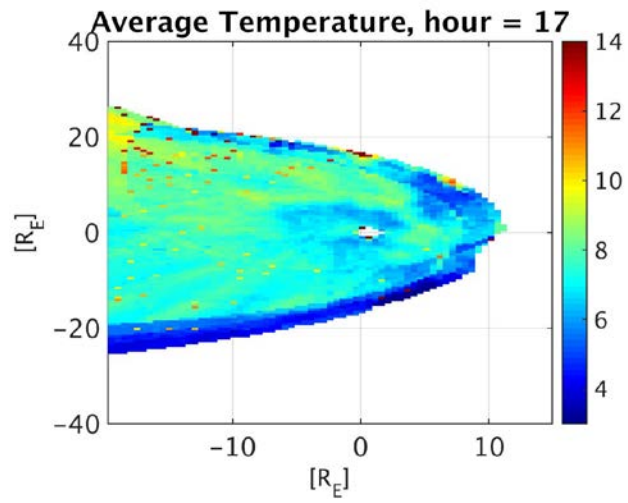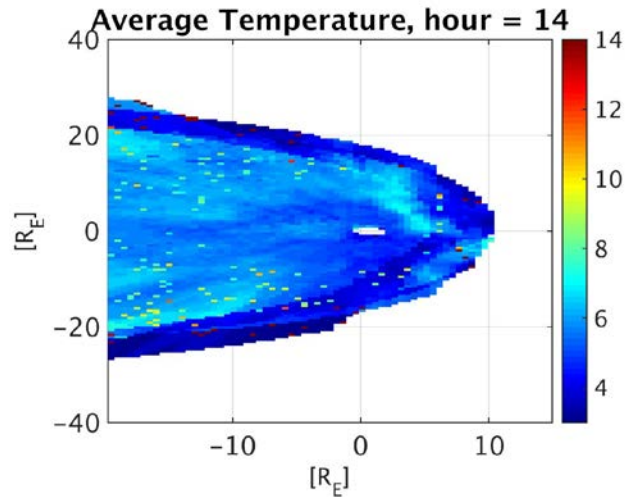
At the start of the initial phase, there is a spike in solar wind dynamic pressure associated with a positive jump in Dst. This feature is observed on average, despite the SSC not being a requirement for storm selection. This is followed by a flip to negative IMF Bz related to the main phase of the storm and the decay in Dst. After the peak of the storm, all parameters progress toward their pre-storm values.

The superposed epoch result for the TWINS equatorial magnetospheric ion temperature data contains a lot of spatial and temporal information. Figure 3 presents the average ion temperature in GSM coordinates at three epoch times in the main phase. The panels in Figure 3 show the average ion temperature at 14, 17, and 20 epoch hours respectively. These plots progress from mid-main phase to storm peak from top to bottom. These three plots highlights how the full magnetospheric ion temperature varies dramatically in time and space with regional heating and cooling at different times.

In each of the three plots in Figure 3, there is a lower temperature in the near-Earth region extending from approximately 1 to 5 R_E. We propose that this could be caused by either the TWINS medium energy range or the sensor head boundary effect. During storm-time near 3 to 5 R_E, we would expect an enhanced, hot 5-60 keV ring current. Since we only examine the 2-32 keV plasma we may be excluding an important population for that region. Incidentally, this is

also the region that results in the largest contributions by the instrumental effects previously described.

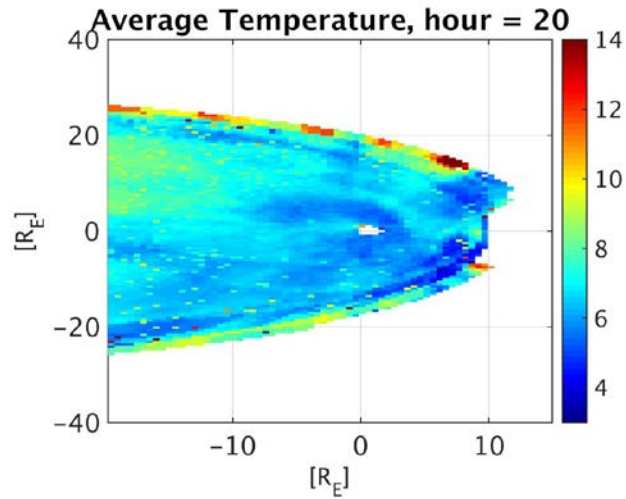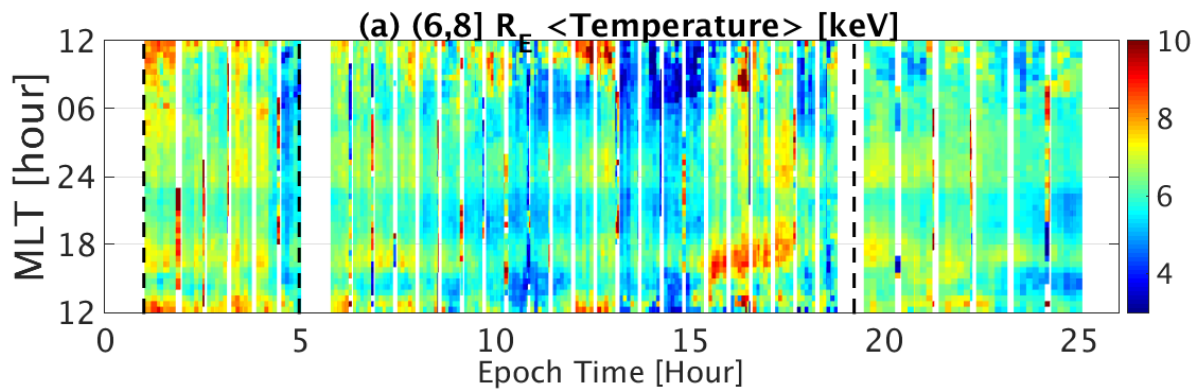Average Temperature, hour = 14

Average Temperature, hour = 17

Figure 3. Superposed epoch average of the equatorially mapped magnetospheric ion temperature at three main phase times (14, 17, and 20 hours) approaching the storm peak. Axis and color are the same as Figure 1.
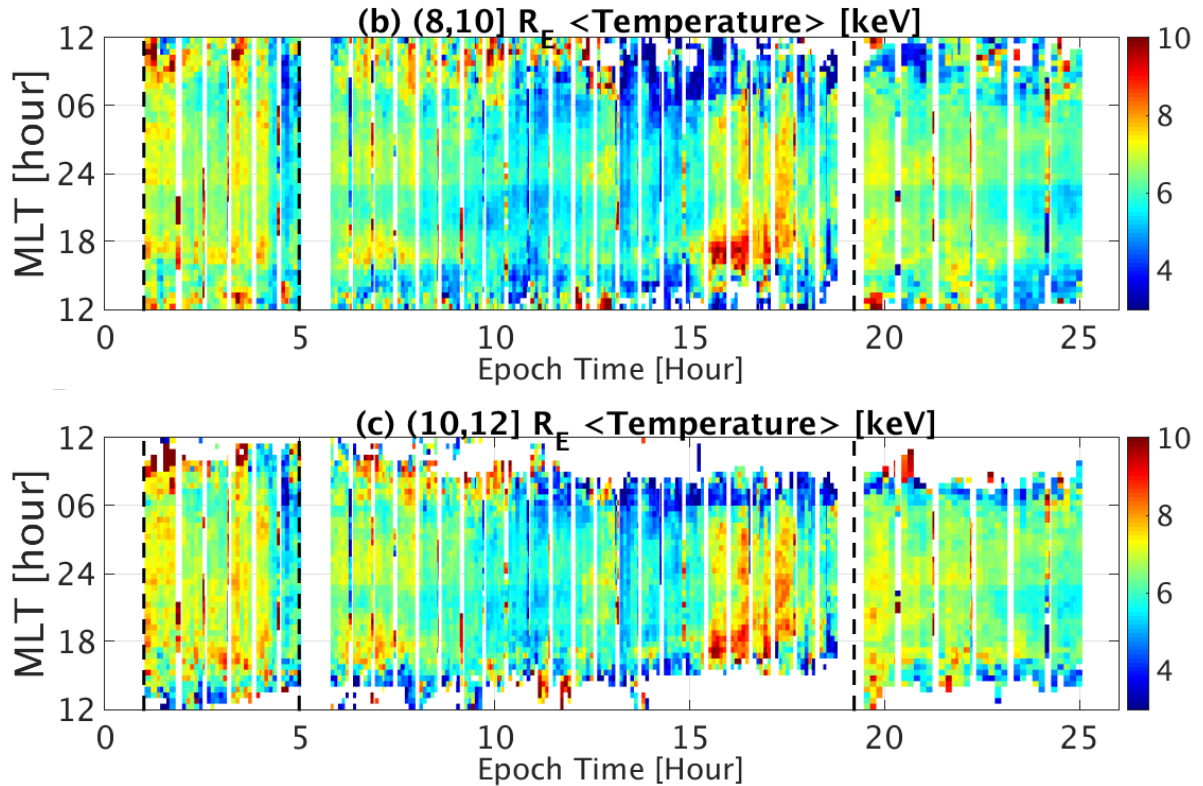
Figure 4. The average ion temperature for three different Lshell ranges; a (6,8] R_E, b (8,10] R_E, and c (10,12] R_E as a function of MLT and epoch time. The colorbar describes the average ion temperature. The dashed black lines describe the epoch markers for storm sudden commencement, the start of the main phase, and the storm peak.

Figure 4 describes the average ion temperature as a function of MLT and epoch time for three different Lshell ranges. The dashed lines show the initial phase, start of the main phase, and the storm peak. It should be noted that the recovery phase is cut short in these plots. This is because this method is less accurate during times of less activity. White indicates no data, either due to missing data or being outside of the magnetopause.

The plot with the Lshell range greater than 6 and less than or equal to 8 R_E, denoted (6, 8] R_E, shows results similar to previous work (e.g. Denton and Borovsky, 2008 and Zhang et al.,

2005) with LANL MPA. The temperature enhances near 18 epoch hours and extends from 14 to 18 MLT hours. The plots displaying the (8, 10] R_E and (10, 12] R_E range show that the enhancement extends further towards midnight and across the night side as the range moves away from the Earth.

Figure 5 shows the reduction of the Lshell dependent ion temperature to an average across the night side (from 6 to 18 MLT hours) as a function of epoch storm time. The different colors describe the different Lshell ranges. The vertical dashed black lines, from left to right, describe the storm sudden commencement, the beginning of the main phase, and the storm peak. This result includes a 30-minute running average along epoch time.
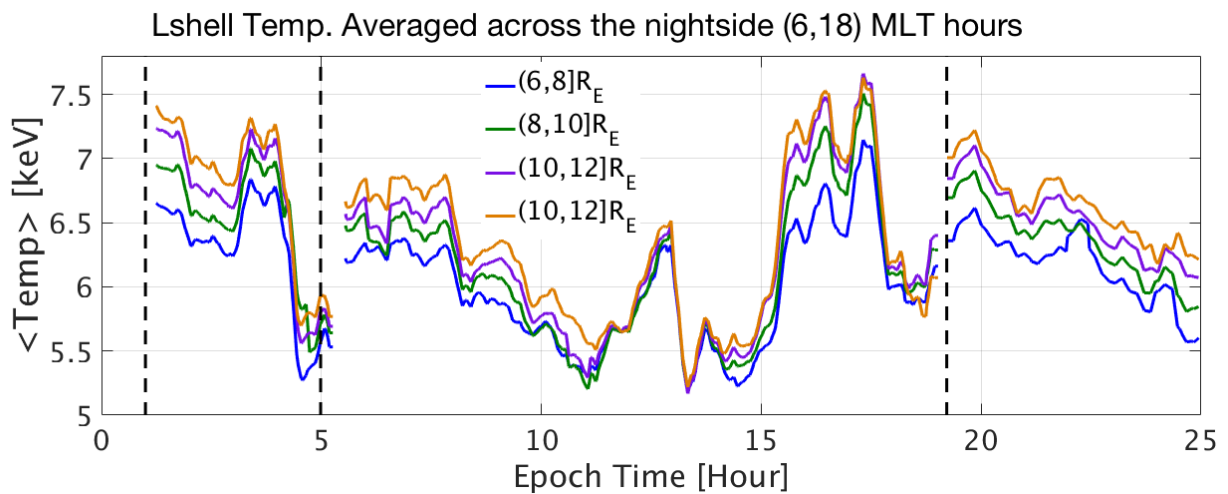

Figure 5. The ion temperature averaged across the night side (6-18 MLT hours) for several Lshell bins as a function of epoch time. The dashed black lines describe the epoch markers for storm sudden commencement, the start of the main phase, and the storm peak.

Figure 5 shows that the night side averages at different Lshells all typically trend together with epoch storm time. The main difference between the Lshell bins is that the smaller Lshells are sometimes cooler than the larger Lshell bins, particularly during times of increased

temperature. To quantify the significance of this separation in average ion temperature, we conducted a T test between each Lshell bin. The T test results are shown in Table 1 in H/P format. An outcome of H = 0 and P = 1, indicated in the table by (0/1), indicates that we accept the null hypothesis that the means of the distribution are the same. This is expected for any comparison of a group to itself. An outcome of H = 1 and P = 0, indicated in the table by (1/0), indicates that we reject the null hypothesis, the means of the distributions are not the same. Table 1 in conjunction with Figure 5 show that there exists a peak in night side ion temperature in the near Earth plasma sheet, between 10 and 14 R_E. Furthermore this peak is statistically significantly larger than the values between 6 and 10 R_E.

Table 1. The Student T test H and P values for each night side Lshell bin.

H/P Values	(6, 8] R_E	(8,10] R_E	(10,12] R_E	(12,14] R_E
(6, 8] R_E	0/1	1/0	1/0	1/0
(8,10] R_E	1/0	0/1	1/0	1/0
(10,12] R_E	1/0	1/0	0/1	0/1
(12, 14] R_E	1/0	1/0	0/1	0/1

6. Validation

To validate the TWINS magnetospheric ion temperature data, we use two approaches. First we conduct an error analysis using Geotail data. Second we examine the storm-time trend using previously published statistical LANL MPA data.

While Geotail was initially chartered to survey the magnetotail, the spacecraft has been surveying the near-Earth magnetotail (-9 > X_{GSM} > -50 R_E) since November 1994. The Low Energy Particle Energy Analyzer (LEP-EA) consists of two nested sets of quadrispherical electrostatic analyzers that measure three-dimensional velocity distributions of hot plasmas in the magnetosphere [*Mukai et al.*, 1994]. The Energy Analyzer for ions (EA-i) has an energy range from 32 eV/q to 39 keV/q within the magnetosphere and 5 keV/Q to 43 keV/Q in the solar wind

region.

In comparing the TWINS and Geotail temperature data, we must consider the differences between the datasets. The observations used in each ion temperature calculation have drastically different energy ranges (i.e. much lower energies included in Geotail). Furthermore, the method of calculation of the total ion temperature, given the different energy range, adds an additional source of error. Additionally, the Geotail data has high temporal and spatial resolution, mapped onto the TWINS grid, which has ten-minute temporal resolution and spatial resolution that is a function of the field of view. Hence, while we see similar trends and magnitudes, we expect a moderate root-mean-square error (RMSE).

The most direct comparison of the two data sets can be optimized methodically. First, since TWINS maps to the hottest value along the LOS, we select the highest value of the Geotail ion temperature in the ten-minute interval. Then, we reduce the Geotail data to only times when Z (in GSM) is less than 5 R_E. Next, we reduce the Geotail data to only times when we have TWINS data at the location where Geotail data maps.

Figure 6 presents the results of the TWINS to Geotail comparison. The left plot (a.) shows all of the Geotail data when and where there is TWINS data and (b.) shows the TWINS data at the concurrent times and locations. In each of these two plots the x-axis is in years, describing the entire possible data set, in one week by 1 keV bins. The color describes the number of points in each. Plot (c.) shows the location of Geotail when and where we have TWINS data in GSM coordinates and 0.5 R_E bins.

To find the RMSE we use the formula $RMSE = \sqrt{\frac{\sum_{s=1}^{n}(twins_s - geotail_s)^2}{n}}$ where n is the number of points and the subscripts $twins_s$ and $geotail_s$ denote the individual TWINS and Geotail ion temperature values. For our RMSE calculation, $n = 5117$, times when the ten-minute resolution data overlaps, and this gives us RMSE = 2.88 keV. Considering the different energy ranges and method of calculation, the error is relatively low.

Figure 6 (d.) presents the mean ion temperature at all locations for both sets of data along epoch time. This plot shows that while the difference between the means is often around 2 keV, with Geotail values being lower than those from TWINS. This consistent difference is expected due to the observational energy range and the method of calculation. The largest error comes in the late recovery phase, which is also expected since the TWINS ENA flux method has a large error at quiet times, with minimum flux.

Figure 6. (a). Geotail ion temperature data when and where we have TWINS data. (b) The corresponding TWINS ion temperature when and where we have Geotail data. (c) The location

of the overlapping data. (d) The mean overlapping TWINS and Geotail data superposed along normalized epoch time (averaged over all locations).

The magnetospheric plasma analyzer (MPA) instruments on board the Los Alamos National Laboratory (LANL) satellites have previously provided plasma observations. These seven satellites orbit near the geographic equatorial plane and make observations at different geographic longitudes. The MPA instrument is a spherical-sector electrostatic analyzer, which measures three-dimensional distributions of ions on timescales of 86 s [*Bame et al.*, 1993]. The energy ranges from 1 eV/q up to 40 keV/q in 40 levels. The spin-averaged fluxes for each energy channel and plasma distributions can be used to calculate the three-dimensional temperature matrix [*Thomsen et al.,* 1996a, 1999].

Qualitative comparison of previous studies using MLT dependent storm time superposed LANL MPA data [e.g. *Denton and Borovsky*, 2008 and *Zhang et al.,* 2006] show that the magnitude and trend of the total ion temperatures at geosynchronous orbit are in excellent agreement. Results from both *Denton and Borovsky*, 2008 and *Zhang et al.,* 2006 show that the average geosynchronous ion temperatures range from approximately 3 to 10 keV during storm time. In particular, approaching the peak of the storm: the hottest ion temperatures (near 10 keV) occur between dusk and noon, moderate ion temperatures (near 8 keV) occur between midnight and dusk, and cooler temperatures (near 5 keV) occur between dawn and midnight, and the coldest (near 3 keV) occur between noon and dawn. These MLT dependent values are a perfect match to what we find using TWINS maps at geosynchronous orbit. Unfortunately, without access to MPA data since 2008, we are not able to conduct a direct comparison.

7. Discussion and Conclusion

The magnetospheric ion temperature data from TWINS ENA flux provides a global view not available with in situ or even multi-spacecraft missions. This method provides an extraordinary result describing the equatorial ion temperature as a function of storm time.

Previous work uses multi-satellite missions to describe only one region, such as geosynchronous orbit. This study uses previous work for validation and extends the result from the inner magnetosphere to the magnetotail.

In this study we present a valuable new data set for 48 moderate to intense (*Dst* < -60 nT) geomagnetic storms that occur between July of 2009 and December 2015. We then quantitatively compare the result to existing Geotail data. Additionally, we validate the TWINS magnetospheric ion temperature by discussing a qualitative comparison to the previous studies using LANL MPA data that is currently unavailable on a large scale. The TWINS ion temperature data expands the view out from geosynchronous orbit through the plasma sheet to the tail.

Figure 4 presents MLT dependent ion temperature as a function of epoch storm time for three Lshell bins extending from the geosynchronous orbit into the plasma sheet. These plots present a peak in the ion temperature near dusk that extends wider in MLT as the view moves away from the Earth.

The difference in the night side ion temperature at different Lshell bins is described in Figure 5. Figure 5 shows that while each Lshell bin follows a similar trend, the inner magnetosphere Lshell bins are typically cooler than the near Earth plasma sheet Lshell bins. The difference between these inner magnetosphere and plasma sheet bins are then shown to be statistically significantly different in Table 1 using two-sample T tests.

The MLT extension of the peak ion temperature shows that during the 48 moderate to intense storms, the hottest equatorial region occurs at approximately an Lshell of 12 R_E. This is farther out than the expected inner magnetosphere and plasma sheet boundary. This distance implies that the hottest ions are not being convected deeply, i.e. into the inner magnetosphere. Contribution from ions above 20 keV to temperature becomes more important with decreasing radial distance, e.g. *Wang et al.* [2011]. It is likely that ENA temperature underestimates the real temperature at smaller radial distances. Moreover, intense storms may produce lower temperatures due to the significant oxygen component in the plasma sheet typical for these storms [*Denton et al.*, 2006]. This effect appears as a higher flux of low energy protons in the measurements. To minimize this

error, *Valek et al.*, 2013 quantified the oxygen contribution to the TWINS flux data and its effect on the temperature calculation.

While this result is obviously apparent using the TWINS ion temperature it should be further investigated using models and assimilated data sets. This additional investigation is necessary when considering the instrumental effect appearing at the boundary of the two sensor heads. The equatorial ion temperature should also be examined as a function of solar wind driver and storm intensity to understand the factors that affect the magnitude and location of the peak enhancement.

In this paper we present the equatorial magnetospheric ion temperature data derived from TWINS ENA flux observations for 48 moderate to intense geomagnetic storms. The TWINS ion temperature data is validated using Geotail and LANL ion temperature data. The TWINS data is then examined statistically using normalized superposed epoch analysis. It is found that the largest MLT extension of the equatorial ion temperature enhancement occurs near 12 R_E.
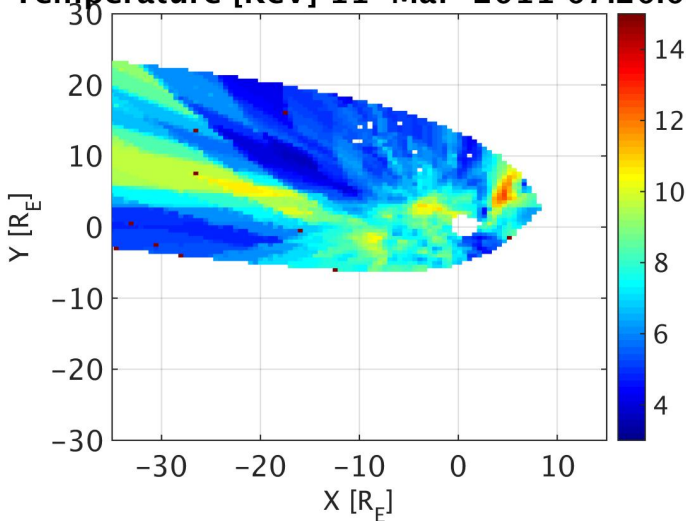
Acknowledgements

References

Bame, S. J., D. J. McComas, M. F. Thomsen, B. L. Barraclough, R. C. Elphic, and J. P. Glore (1993), Magnetospheric plasma analyzer for spacecraft with constrained resources, *Rev. Sci. Instrum.*, 64, 1026–1033.

Baumjohann, W. (1993), The near-Earth plasma sheet: An AMPTE/IRM perspective, *Space Sci. Rev.,* 64, 141–163.

Baumjohann, W., G. Paschmann, and C. A. Cattell (1989), Average plasma properties in the central plasma sheet, *J. Geophys. Res.,* 94, 6597–6606.

Birn, J., Thomsen, M. F., Borovsky, J. E., Reeves, G. D., McComas, D. J., and Belian, R. D. (1997), Characteristic

plasma properties of dispersionless substorm injections at geosynchronous orbit, J. Geophys. Res., 102, 15,345.

Borovsky, J. E., M. F. Thomsen, and D. J. McComas (1997), The superdense plasma sheet: Plasmaspheric origin, solar wind origin, or ionospheric origin?, J. Geophys. Res., 102, 22,089.

Chen, M. W., L. R. Lyons, and M. Schulz (1994), Simulations of phase space distributions of storm time proton ring current, *J. Geophys. Res.,* 99, 5745–5759.

Denton, M. H., and J. E. Borovsky (2008), Superposed epoch analysis of high-speed-stream effects at geosynchronous orbit: Hot plasma, cold plasma, and the solar wind, *J. Geophys. Res.,* 113, A07216, doi:10.1029/2007JA012998.

Denton, M. H., M. F. Thomsen, H. Korth, S. Lynch, J. C. Zhang, and M. W. Liemohn (2005), Bulk plasma properties at geosynchronous orbit, *J. Geophys. Res.*, 110, A07223, doi:10.1029/2004JA010861.

Denton, M. H., J. E. Borovsky, R. M. Skoug, M. F. Thomsen, B. Lavraud, M. G. Henderson, R. L. McPherron, J.-C. Zhang, and M. W. Liemohn (2006), Geomagnetic disturbances driven by ICME- and CIR- dominated solar wind, *J. Geophys. Res.,* 111, A07S07, doi:10.1029/2005JA011436.

Ebihara, Y., M.-C. Fok, R. A. Wolf, M. F. Thomsen, and T. E. Moore (2005), Nonlinear impact of plasma sheet density on the storm-time ring current, *J. Geophys. Res.,* 110, A02208, doi:10.1029/2004JA010435.

Friedel, R. H. W., H. Korth, M. G. Henderson, M. F. Thomsen, and J. D. Scudder (2001), Plasma sheet access to the inner magnetosphere, *J. Geophys. Res.*, 106, 5845– 5858.

Goldstein, J., & McComas, D. J. (2013). Five years of stereo magnetospheric imaging by TWINS. *Space Science Reviews*, *180*(1-4), 39-70.

Hughes, W. J. (1995), The magnetopause, magnetotail, and magnetic reconnection, in *Introduction to Space Physics*, edited by M. G. Kivelson and C. T. Russell, pp. 227–287, Cambridge Univ. Press, New York.

Katus, R. M., et al., (2015), Statistical analysis of the geomagnetic response to different solar wind drivers and the dependence on storm intensity, *J. Geophys. Res. Space Physics*, 120, 310–327, doi:10.1002/2014JA020712.

Katus, R. M. and M. W. Liemohn (2013), Similarities and differences in low- to middle -latitude geomagnetic indices, *J. Geophys. Res. Space Physics*, 118, doi:10.1002/jgra.50501.

Katus, R. M., et al., (2013), Normalized superposed epoch analysis reveals two-step main phase enhancement: evidence for potential and inductive convection during intense geomagnetic events, *J. Geophys. Res.*, 2012JA017915.

Keesee, A. M., Elfritz, J. G., Fok, M. C., McComas, D. J., & Scime, E. E. (2014). Superposed epoch analyses of ion temperatures during CME-and CIR/HSS-driven storms. *Journal of Atmospheric and Solar-Terrestrial Physics*, *115*, 67-78.
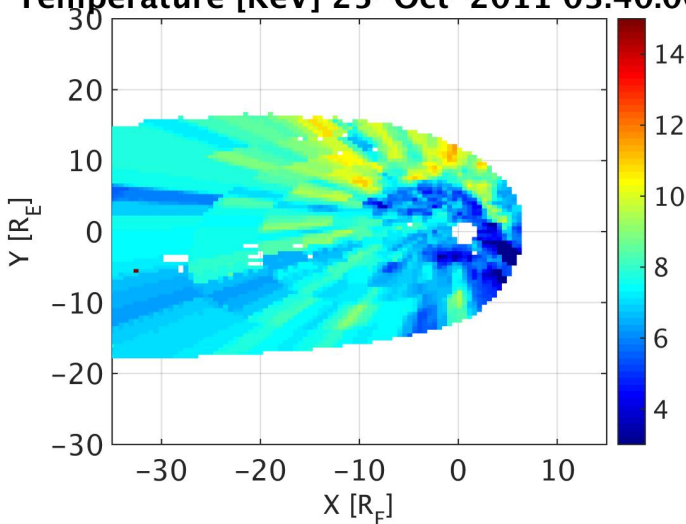
Keesee, A. M., J. G. Elfritz, D. J. McComas, and E. E. Scime (2012), Inner magnetosphere convection and magnetotail structure of hot ions imaged by ENA during a HSS-driven storm, *J. Geophys. Res.*, 117, A00L06, doi:10.1029/2011JA017319.

Korth, H., and M. F. Thomsen (2001), Plasma sheet access to geosynchronous orbit: Generalization to numerical global field models, *J. Geophys. Res.*, 106, 29,655– 29,668.

Korth, H., M. F. Thomsen, J. E., and D. J. McComas (1999), Calculation of moments from measurements by the Los Alamos magnetospheric plasma analyzer, LA Rep. LA-13566-MS, Los Alamos Natl. Lab., Los Alamos, N. M.

Krimigis, S. M., J. W. Kohl, and T. P. Armstrong (1975), The magnetospheric contribution to the quiet-time low energy nucleon spectrum in the vicinity of Earth, *Geophys. Res. Lett.,* 2, 457–460, doi:10.1029/ GL002i010p00457.

Lavraud, B., M. H. Denton, M. F. Thomsen, J. E. Borovsky, and R. H. W. Friedel (2005), Superposed epoch analysis of dense plasma access to geosynchronous orbit, Ann. Geophys., 23, 2519.

Liemohn, M. W., J.-C. Zhang, M. F. Thomsen, J. E. Borovsky, J. U. Kozyra, and R. Ilie (2008), Plasma properties of superstorms at geosynchronous orbit: How different are they?, Geophys. Res. Lett., 35, L06S06, doi:10.1029/2007GL031717.

McComas, D. J., N. Buzulukova, M. G. Connors, M. A. Dayeh, J. Goldstein, H. O. Funsten, S. Fuselier, N. A. Schwadron, and P. Valek (2012), Two Wide-Angle Imaging Neutral-Atom Spectrometers and Interstellar Boundary Explorer energetic neutral atom imaging of the 5 April 2010 substorm, J. Geophys. Res., 117, A03225, doi:10.1029/2011JA017273.

McComas, D. J., et al. (2009), The two wide-angle imaging neutral-atom spectrometers (TWINS) NASA mission-of-opportunity, *Space Sci. Rev.,* 142, 157–231, doi:10.1007/s11214-008-9467-4.

Mukai, T., S. Machida, Y. Saito, M. Hirahara, T. Terasawa, N. Kaya, T. Obara, M. Ejiri, and A. Nishida (1994), The low energy particle (LEP) experiment onboard the GEOTAIL satellite, *J. Geomagn. Geoelec.*, **46**, 669–692.

Ohtani, S., M. A. Shay, and T. Mukai (2004), Temporal structure of the fast convective flow in the plasma sheet: Comparison between observations and two-fluid simulations, *J. Geophys. Res.,* 109, A03210, doi:10.1029/2003JA010002.

Roelof, E. C., and A. J. Skinner (2000), Extraction of ion distributions from magnetospheric ENA and EUV images, *Space Sci. Rev.*, **91**, 437.

Roelof, E. C. (1987), Energetic neutral atom image of a storm-time ring current, *Geophys. Res. Lett.,* 14, 652–655, doi:10.1029/GL014i006p00652.

Roelof, E. C., D. G. Mitchell, and D. J. Williams (1985), Energetic neutral atoms (E ~ 50 keV) from the ring current: IMP 7/8 and ISEE 1, *J. Geophys. Res.,* 90(A11), 10,991–11,008, doi:10.1029/JA090iA11p10991.

Terasawa, T., Fujimoto, M., Mukai, T., Shinohara, I., Saito, Y., Yamamoto, T., Machida, S., Kokubun, S., Lazarus, A.J., Steinberg, J.T. and Lepping, R.P., (1997). Solar wind control of density and temperature in the near-Earth plasma sheet: WIND/GEOTAIL collaboration. *Geophysical Research Letters*, *24*(8), 935-938.

Thomsen, M. F., D. J. McComas, G. D. Reeves, and L. A. Weiss (1996a), An observational test of the Tsyganenko (T89a) model of the magnetospheric field, *J. Geophys. Res.*, 101, 24,827– 24,836.

Thomsen, M. F., J. E. Borovsky, R. M. Skoug, and C. W. Smith (2003), Delivery of cold, dense plasma sheet material into the near-Earth region, *J. Geophys. Res.,* 108(A4), 1151, doi:10.1029/2002JA009544.

Valek, P. W., J. Goldstein, D. J. McComas, M.-C. Fok, and D. G. Mitchell (2014), Large magnetic storms as viewed by TWINS: A study of the differences in the medium energy ENA composition, J. Geophys. Res. Space Physics, 119, 2819–2835, doi:10.1002/2014JA019782.

Wang, C.-P., M. Gkioulidou, L. R. Lyons, R. A. Wolf, V. Angelopoulos, T. Nagai, J. M. Weygand, and A. T. Y. Lui (2011), Spatial distributions of ions and electrons from the plasma sheet to the inner magnetosphere: Comparisons between THEMIS-Geotail statistical results and the Rice convection model, *J. Geophys. Res.,* 116, A11216, doi:10.1029/2011JA016809.

Wang, C.-P., L. R. Lyons, J. M. Weygand, T. Nagai, and R. W. McEntire (2006), Equatorial distributions of the plasma sheet ions, their electric and magnetic drifts, and magnetic fields under different interplanetary magnetic field B_Z conditions, *J. Geophys. Res.,* 111, A04215, doi:10.1029/2005JA011545.

Zhang, J.-C., M. W. Liemohn, M. F. Thomsen, J. U. Kozyra, M. H. Denton, and J. E. Borovsky (2006), A statistical comparison of hot-ion properties at geosynchronous orbit during intense and moderate geomagnetic storms at solar maximum and minimum, *J. Geophys. Res.*, 111, A07206, doi:10.1029/2005JA011559.
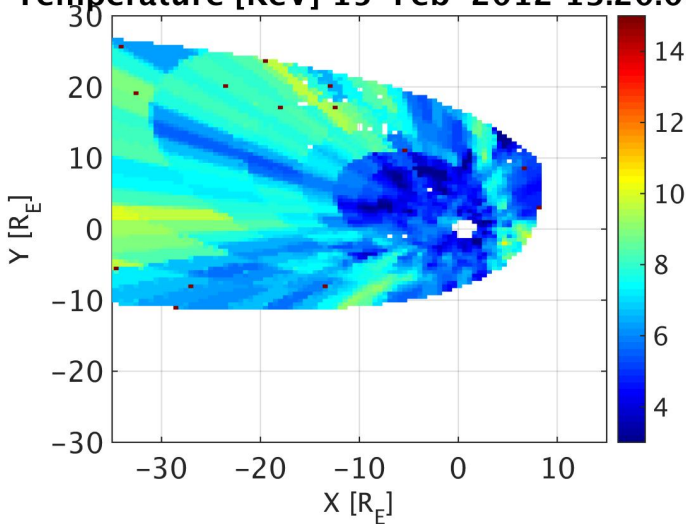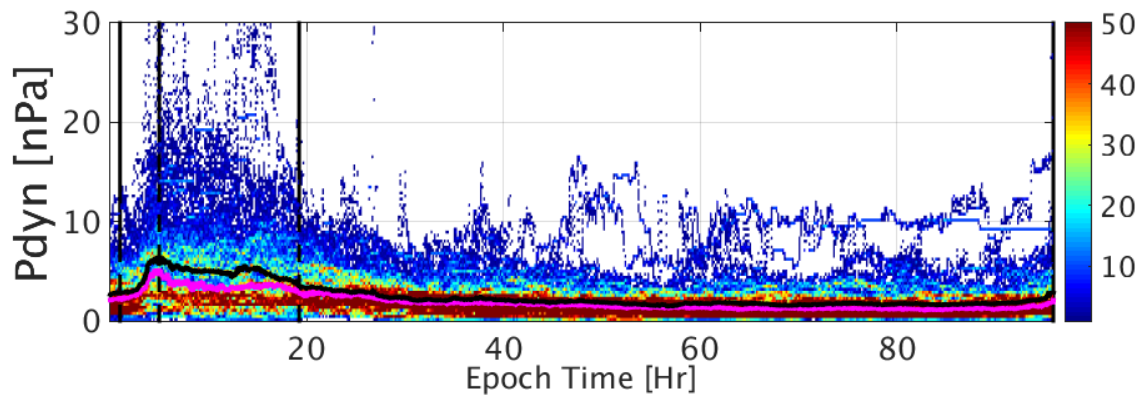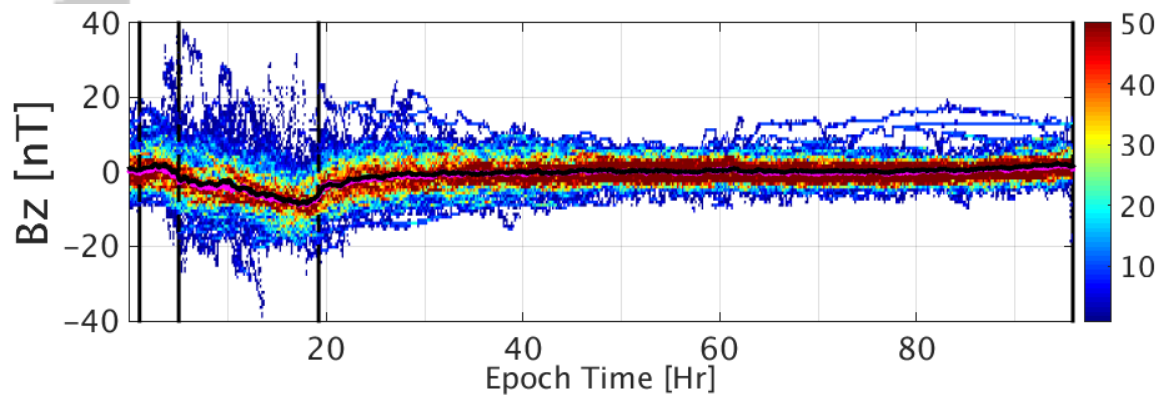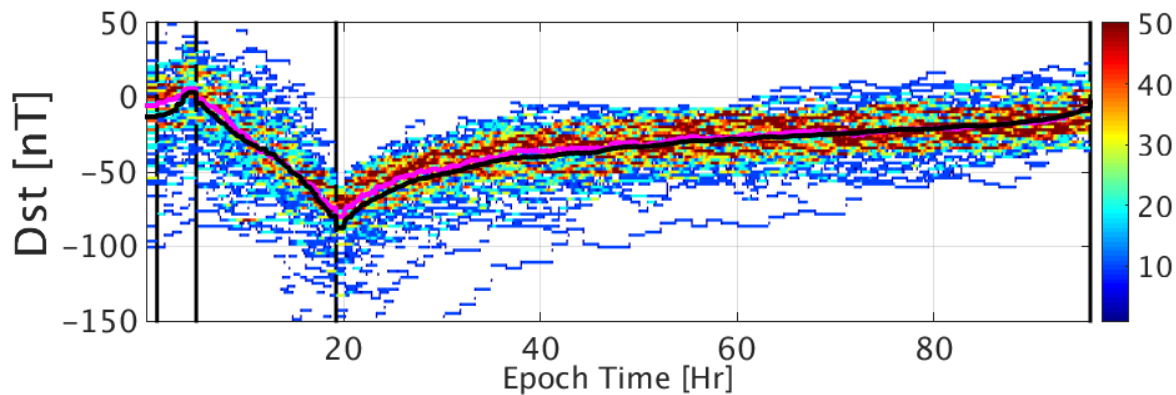
Temperature [KeV] 11−Mar−2011 07:20:00
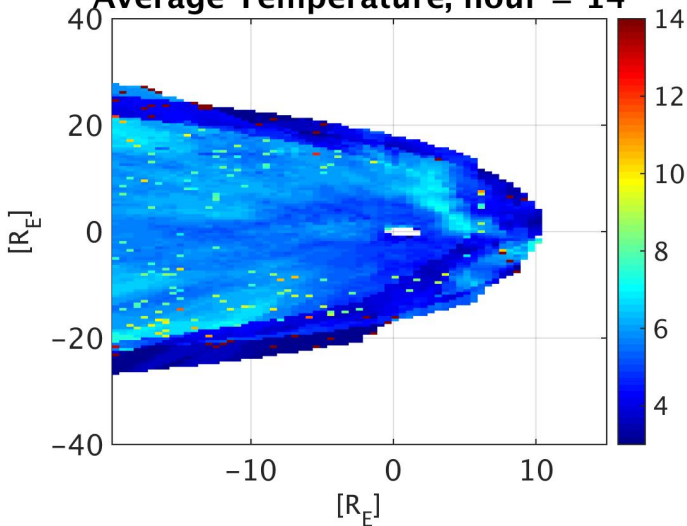

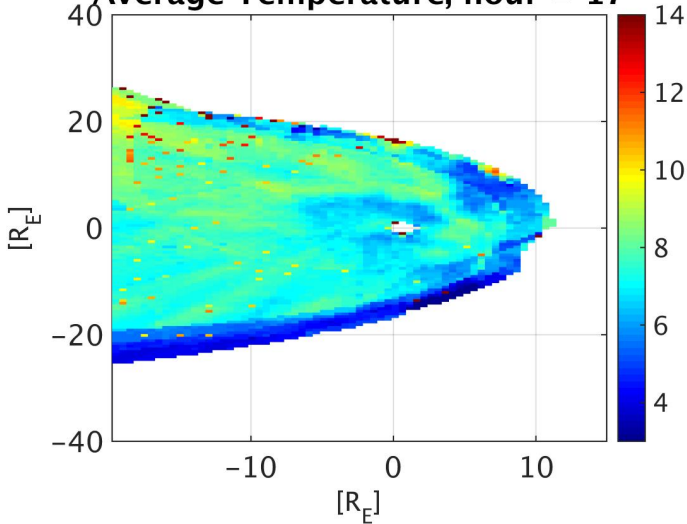Temperature [KeV] 25−Oct−2011 03:40:00
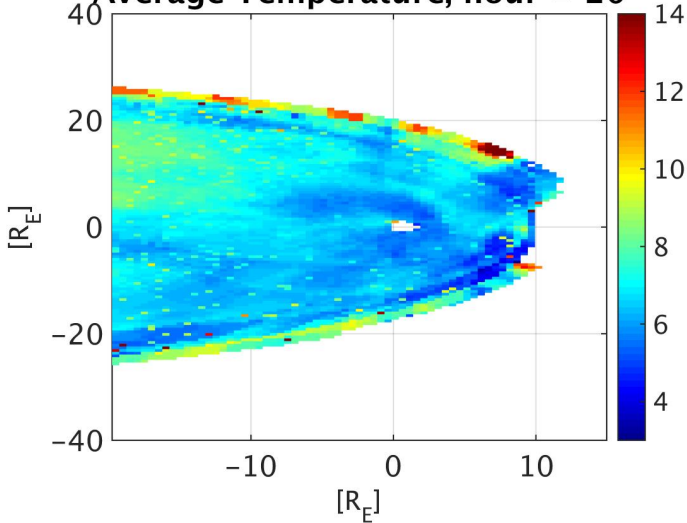

Temperature [KeV] 15−Feb−2012 13:20:00

Average Temperature, hour = 14
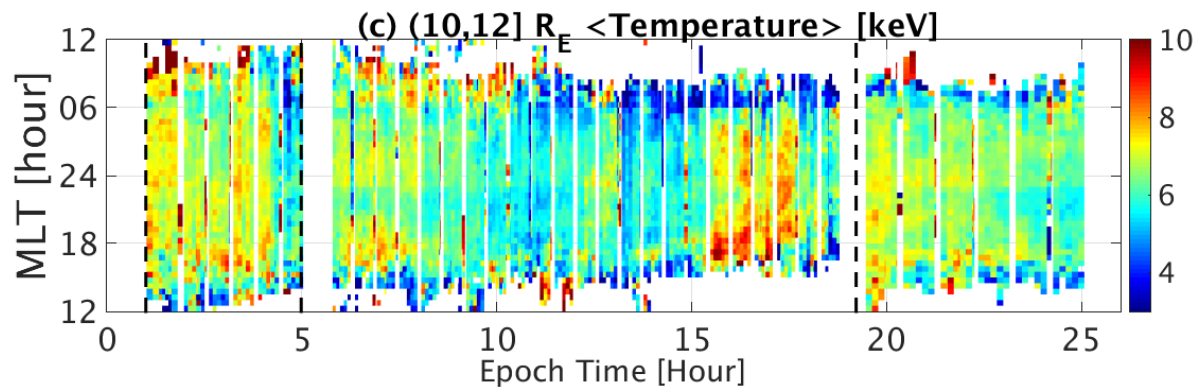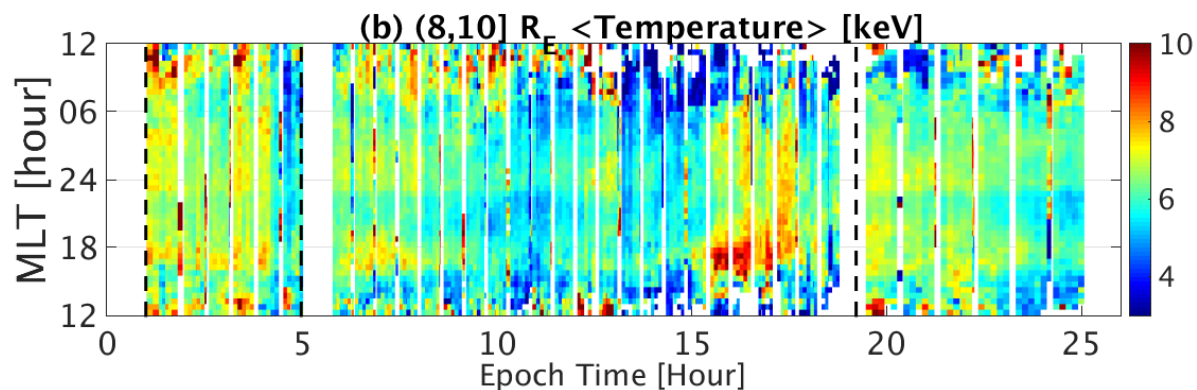
Average Temperature, hour = 17

Average Temperature, hour = 20

(a) (6,8) R_E <Temperature> [keV]

(b) (8,10) R_E <Temperature> [keV]

(c) (10,12) R_E <Temperature> [keV]

Lshell Temp. Averaged across the nightside (6,18) MLT hours

Legend:
- (6,8]R_E
- (8,10]R_E
- (10,12]R_E
- (10,12]R_E

Y-axis: <Temp> [keV]

X-axis: Epoch Time [Hour]

(a) GEOTAIL, when and where there's TWINS

(b) TWINS, when and where there's GEOTAIL

(c) GEOTAIL Location Count

(d) Mean Ion Temperature